ChemComm

COMMUNICATION

View Article Online
View Journal | View Issue

Cite this: *Chem. Commun.*, 2019, 55, 13729

Received 11th September 2019,
Accepted 21st October 2019

DOI: 10.1039/c9cc07108c

rsc.li/chemcomm

$Ti_3C_2/BiVO_4$ Schottky junction as a signal indicator for ultrasensitive photoelectrochemical detection of $VEGF_{165}$†

Yaling Liu, Hongmei Zeng, Yaqin Chai, Ruo Yuan * and Hongyan Liu *

A "signal-on" photoelectrochemical (PEC) biosensor was developed for ultrasensitive detection of vascular endothelial growth factor 165 ($VEGF_{165}$) based on a $Ti_3C_2/BiVO_4$ Schottky junction, which was a novel sensitized structure with excellent photovoltaic performance, prominent film-forming ability and stability. The generation of a built-in electric field by the $Ti_3C_2/BiVO_4$ Schottky junction efficiently suppressed the combination of photogenerated electron–hole pairs and enhanced the photocurrent, providing a high initial photocurrent signal for the construction of a photoelectrochemical (PEC) biosensor.

Photoelectrochemical (PEC) analysis is a technique that combines the merits of photochemistry and electrochemistry, such as easy operation, low cost, simple instruments, high sensitivity and low signal-to-noise ratio.[1–5] For the construction of a PEC sensing platform, the photoactive material is the key component to generate the initial photocurrent response. Nevertheless, single photoactive materials usually suffer from the disadvantage of low photoelectric conversion efficiency. Currently, great effort is being devoted to the construction of co-sensitized systems by combining multiple photoactive materials, thus improving the initial photocurrent signal.[6–8] For example, our group reported a PEC biosensor by using poly{4,8-bis[5-(2-ethylhexyl)thiophen-2-yl]benzo[1,2-*b*:4,5-*b*′]dithiophene-2,6-diyl-*alt*-3-fluoro-2-[(2-ethylhexyl)-carbonyl]thieno[3,4-*b*]thiophene-4,6-diyl} as the photoactive material and polyaniline, fullerene, and perylenetetracarboxyl diimide as the sensitizers.[9] Zhu's group constructed a biosensor by using electrochemically reduced graphene and $ZnIn_2S_4$ to sensitize TiO_2.[10] Although the photoelectric conversion efficiency can be improved by the co-sensitized system, it remains a problem to find the cascade sensitizers with matched energy level gradient and strong interfacial contact. Therefore, it is of great significance to develop a new strategy to improve the photoelectric conversion efficiency of photoactive materials.

MXenes, a family of two-dimensional transition metal carbides, carbonitrides or nitrides, have attracted much concern in batteries, photocatalysis and electrochemistry due to their desirable advantages of high specific surface area, excellent conductivity, adjustable components and controllable minimum thickness of nanometer layer.[11–15] Taking Ti_3C_2 for example, there are abundant hydrophilic functional groups on the surface of Ti_3C_2 (–OH, –F, or –O), which makes it easy to sufficiently interfacially connect with other materials. The excellent metallic electrical conductivity of Ti_3C_2 favors the transfer of electrons. Therefore, Ti_3C_2 has great potential to act as a co-catalyst to enhance the photoelectric conversion efficiency of other photoactive materials. Recently, $BiVO_4$ has emerged as a promising candidate for PEC sensors owing to its narrow band gap of 2.4 eV, superior photoelectric response and nontoxicity.[16] However, $BiVO_4$ suffered from poor electron mobility, high recombination of electrons and holes and low photoelectric conversion efficiency.[17] Accordingly, considering the remarkable merits of Ti_3C_2, it is anticipated that the combination of Ti_3C_2 with $BiVO_4$ can dramatically improve the PEC performance of $BiVO_4$. The Ti_3C_2–$BiVO_4$ interface may form a Schottky junction due to the excellent metallic conductivity of Ti_3C_2 MXenes,[18,19] followed by the generation of a built-in electric field.[20,21] Therefore, the light-generated electrons of $BiVO_4$ can be timely transported to the surface of Ti_3C_2 *via* the built-in electric field, suppressing the combination of photogenerated electron–hole pairs and enhancing the photocurrent.[22] Therefore, the design of a Ti_3C_2 based Schottky junction could not only improve the photoelectric conversion efficiency of the photoactive materials without considering the matching of the band level, but also provide an excellent interfacial contact to facilitate the electron transfer, generating a high initial photocurrent signal for the construction of the PEC biosensor.

Herein, a novel PEC biosensor for ultrasensitive detection of $VEGF_{165}$, an important biomarker related to various diseases such as lung cancer and breast cancer,[23–25] was developed by

Key Laboratory of Luminescent and Real-Time Analytical Chemistry (Southwest University), Ministry of Education, College of Chemistry and Chemical Engineering, Southwest University, Chongqing 400715, P. R. China.
E-mail: liuhy860@swu.edu.cn, yuanruo@swu.edu.cn; Fax: +86-23-68253172; Tel: +86-23-68252277

† Electronic supplementary information (ESI) available: Experimental details and electrochemical characterizations. See DOI: 10.1039/c9cc07108c

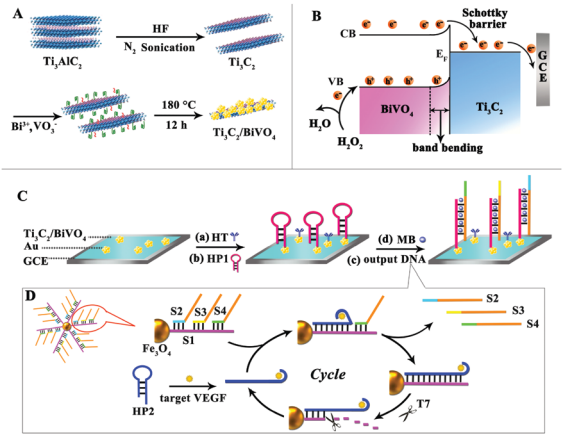

Scheme 1 (A) Preparation of the $Ti_3C_2/BiVO_4$ photoactive material; (B) the electron transfer mechanism of the $Ti_3C_2/BiVO_4$ Schottky junction; (C) the fabrication process of the PEC biosensor; (D) the target-induced enzyme-assisted dual signal amplification procedure.

using a $Ti_3C_2/BiVO_4$ Schottky junction as the signal indicator. As shown in Scheme 1, the $Ti_3C_2/BiVO_4$ nanocomposite was synthesized by *in situ* growth of $BiVO_4$ on Ti_3C_2 and coated on the electrode to produce an initial photocurrent signal. To further improve the detection sensitivity of the PEC sensor, a T7 Exonuclease (T7 Exo)-assisted target $VEGF_{165}$-induced dual signal amplification strategy was employed. With the target $VEGF_{165}$, the hairpin DNA (HP2), containing the aptamer of $VEGF_{165}$ can be specifically identified and opened to specifically recognize the exposed toehold of S1 on the magnetic bead, releasing the output DNA S2, S3, and S4. In addition, T7 Exo was used to digest the recessed 5' termini of double-stranded DNA (dsDNA). $VEGF_{165}$-HP2 complex was released for the next cycle, which can be converted to multiple output DNAs. Subsequently, the output DNA can hybridize with hairpin DNA (HP1) on the electrode to form a double-stranded structure, which provided a wonderful platform for the intercalation of MB. MB can effectively increase light absorption and promote the electron transfer along the dsDNA,[25] resulting in an enhanced PEC signal. Consequently, the increase of the photocurrent signal was related to the concentration of $VEGF_{165}$, which can quantitatively detect $VEGF_{165}$. The constructed biosensor provided a new platform for highly sensitive detection of biomarkers for clinical diagnosis.

Scanning electron microscopy (SEM) and transmission electron microscopy (TEM) were employed to characterize the morphology of $Ti_3C_2/BiVO_4$. As shown in Fig. S5 (ESI†), Ti_3C_2 shows broad sheet morphology. For the $Ti_3C_2/BiVO_4$ composite, it can be clearly observed that the $BiVO_4$ particles were wrapped on the Ti_3C_2 sheet (Fig. 1A and B) due to the electrostatic assembly of negatively charged Ti_3C_2 sheets and positively charged Bi^{3+}. High-resolution TEM shows that $Ti_3C_2/BiVO_4$ displayed clear lattice fringes. As shown in Fig. 1C, $Ti_3C_2/BiVO_4$ showed a lattice distance of 1 nm, corresponding to the (002) plane of Ti_3C_2. The lattice distance of 0.29 nm corresponds to the (040) plane of $BiVO_4$. The results suggested that a nanoscale junction was formed. In addition, high angle annular dark field scanning transmission electron microscopy (HAADF-STEM) showed the element mapping of

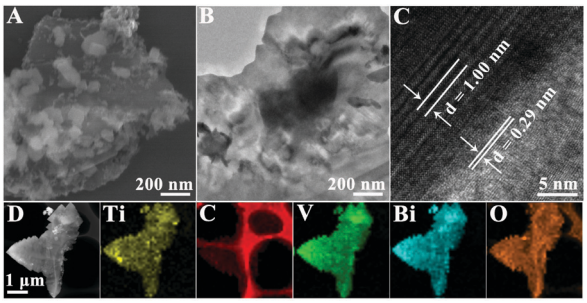

Fig. 1 (A) SEM image of $Ti_3C_2/BiVO_4$; (B) TEM image of $Ti_3C_2/BiVO_4$; (C) HRTEM image of $Ti_3C_2/BiVO_4$; (D) the element mappings of Ti, C, V, Bi, and O of $Ti_3C_2/BiVO_4$.

$Ti_3C_2/BiVO_4$, indicating the existence and homogeneous distribution of C, Ti, O, Bi and V elements. Obviously, compared with the Ti and C elements, the greater densities of V, Bi, and O elements on the Ti_3C_2 external surface imply that the Ti_3C_2 was wrapped by $BiVO_4$.

X-ray diffraction (XRD) was used to analyze the crystal structure of the prepared materials. As depicted in Fig. S6A (ESI†), after reaction of Ti_3AlC_2 with HF, the diffraction peaks at 9.5°, 18.4°, 27.7°, 34.1°, 42.0° and 60.9° correspond to the (002), (004), (006), (101), (105) and (110) reflection of Ti_3C_2. Compared with Ti_3AlC_2, the diffraction peak of (104) at 39° completely disappeared and the peaks of (002) at 9.2° and (004) at 18.4° were shifted to the lower angle side and became broader, illustrating the removal of Al. The XRD patterns of $BiVO_4$ and $Ti_3C_2/BiVO_4$ showed similar profiles. The peaks located at 18.9°, 28.8°, 30.6°, 34.4°, 35.2°, 39.8°, 42.4°, 47.3°, 50.3° and 53.3° were distinctly indexed, respectively, to the (001), (−121), (040), (200), (002), (211), (051), (042), (202) and (161) crystal planes of $BiVO_4$ (JPCDS No. 14-688). The $Ti_3C_2/BiVO_4$ showed decreased intensities as compared to pristine $BiVO_4$ (Fig. S6B, ESI†). X-ray photoelectron spectroscopy (XPS) analysis was applied to further investigate the chemical state of the as-prepared samples. The survey XPS spectra of Ti_3C_2, $BiVO_4$ and $Ti_3C_2/BiVO_4$ are shown in Fig. S7A (ESI†). The survey XPS spectrum of $Ti_3C_2/BiVO_4$ clearly showed the elements of Bi, V, O, Ti and C. Ti_3C_2 exhibits four characteristic peaks at 281.8 eV, 284.8 eV, 286.7 eV, and 288.9 eV, respectively corresponding to Ti–C, C–C, C–O and C–F bonds. After the formation of $BiVO_4$ on Ti_3C_2, the peaks of Ti–C completely disappeared, implying that Ti–C bond was broken in the process of synthesis (Fig. S7B, ESI†). In addition, the low valence Ti peak disappeared, indicating that an intense redox reaction took place in the process of synthesis because of the consumption of the low valence Ti peak (Fig. S7C, ESI†).

Fig. 2 shows the photocurrent intensity of Ti_3C_2, $BiVO_4$ and the $Ti_3C_2/BiVO_4$ composite with different percentages of Ti_3C_2. Obviously, there was nearly no photocurrent response for Ti_3C_2 (curve a). The photocurrent intensity of $BiVO_4$ was 0.506 μA (curve b). There was an apparent enhancement of the photocurrent signal after Ti_3C_2 was combined. The signal was 1.030 μA and 1.207 μA for 1% and 2% Ti_3C_2, respectively (curve c, d). However, the photocurrent intensity of 5% $Ti_3C_2/BiVO_4$ was decreased to 0.612 μA (curve e). Briefly, when the content of

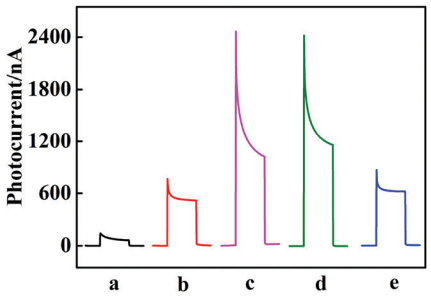

Fig. 2 PEC response of the materials: (a) Ti_3C_2, (b) $BiVO_4$, (c) 1% Ti_3C_2/$BiVO_4$, (d) 2% Ti_3C_2/$BiVO_4$ and (e) 5% Ti_3C_2/$BiVO_4$.

Ti_3C_2 was 1% and 2%, it played the role of a mediator to transfer the electrons. As shown in Scheme 1B, the electrons can transfer from the valence band (VB) of $BiVO_4$ to the conduction band (CB) under illumination, generating electron hole pairs. The electrons transfer from $BiVO_4$ to Ti_3C_2 *via* the built-in electric field to reduce the recombination of electrons and holes, thus increasing the photocurrent response. However, when the content of Ti_3C_2 was 5%, the lower content of photoactive material $BiVO_4$ caused the decrease of the photocurrent response. Therefore, 2% Ti_3C_2/$BiVO_4$ was chosen for the further construction of the PEC biosensor.

The analytical performance of the biosensor was investigated *via* quantitative detection of $VEGF_{165}$. As observed in Fig. 3A, the photocurrent signal increased with an increase of $VEGF_{165}$ concentration from 10 fM to100 nM. Fig. 3B showed a good linear relationship between the logarithm of the $VEGF_{165}$ concentration and the PEC signal. The regression equation for $VEGF_{165}$ was $I = 0.1206 \lg c + 1.750$, ($r = 0.9975$), in which I represented the PEC signal, c represented the concentration of $VEGF_{165}$ and r represented the correlation coefficient. The detection limit of $VEGF_{165}$ was 3.3 fM. Besides, there was a comparison of the biosensor with the reported methods, as shown in Table S2 (ESI†), indicating that the proposed biosensor exhibited wider linear range and lower detection limit.

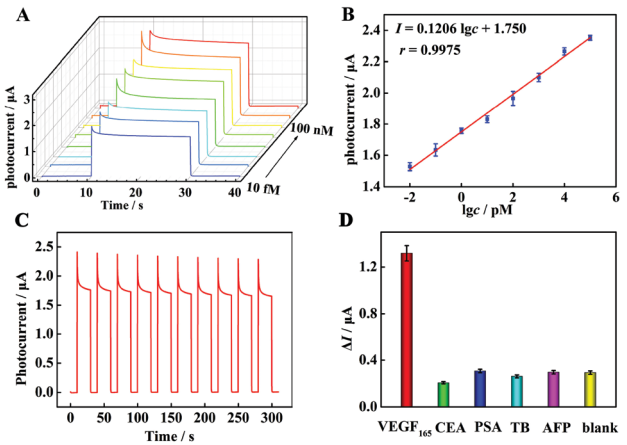

Fig. 3 (A) Photocurrent response of the biosensor incubated with $VEGF_{165}$ of different concentrations; (B) calibration curve between the logarithm of $VEGF_{165}$ concentration and photocurrent; (c) stability of the proposed biosensor under consecutive off–on–off light for 10 cycles; (d) selectivity of the fabricated biosensor toward interferents: CEA, PSA, TB, AFP, and the blank.

The stability of the PEC biosensor was investigated by continuous scanning for 10 cycles. As can be seen in Fig. 3C, the PEC signal was fairly stable in the process of testing. The relative standard deviation (RSD) of 2.26% was acquired, which indicated the excellent stability of the PEC biosensor. Moreover, the selectivity toward $VEGF_{165}$ was also investigated by utilizing carcinoembryonic antigen (CEA), prostate specific antigen (PSA), thrombin (TB) and alpha-fetal protein (AFP) as interferents. As shown in Fig. 3D, there was no obvious enhancement of the PEC signal in the presence of 100 nM interferents. However, the PEC signal corresponding to $VEGF_{165}$ with a lower concentration of 10 nM displayed an apparent enhancement. The result of blank detection was similar to that of the interferent detection. The results revealed the high selectivity of the biosensor for $VEGF_{165}$. Meanwhile, the inter-assay and intra-assay reproducibility was estimated (Fig. S8, ESI†). The inter-assay and intra-assay RSD values were calculated to be 2.42% and 2.26%, respectively, illustrating the outstanding reproducibility of the biosensor.

In summary, we developed a ''signal-on'' PEC strategy by using a Ti_3C_2/$BiVO_4$ Schottky junction as a signal indicator for ultrasensitive detection of $VEGF_{165}$. The Ti_3C_2/$BiVO_4$ displayed outstanding photovoltaic performances compared to the pristine $BiVO_4$, owing to the formation of a Schottky junction, which promoted the separation and transportation of electrons. With the aid of a target-induced enzyme-assisted dual cycling amplification strategy, the detection sensitivity of the PEC biosensor was further improved. More importantly, the construction strategy of the biosensor can be extended to detect other targets in biological analysis and disease diagnosis.

This work was financially supported by the National Natural Science Foundation of China (21501081) and the Fundamental Research Funds for the Central Universities (XDJK2017C021, and XDJK2018AA003).

Conflicts of interest

There are no conflicts to declare.

Notes and references

1 Y. F. Tang, X. Q. Liu, H. J. Zheng, L. W. Yang, L. L. Li, S. Zhang, Y. M. Zhou and S. Alwarappan, *Nanoscale*, 2019, **11**, 9115–9124.
2 J. Wang, M. M. Song, C. G. Hu and K. B. Wu, *Anal. Chem.*, 2018, **90**, 9366–9373.
3 L. X. Meng, Y. M. Li, R. Y. Yang, X. H. Zhang, C. C. Du and J. H. Chen, *Chem. Commun.*, 2019, **55**, 2182–2185.
4 T. Hou, N. N. Xu, W. X. Wang, L. Ge and F. Li, *Anal. Chem.*, 2018, **90**, 9591–9597.
5 F. J. Han, Z. Q. Song, M. H. Nawaz, M. J. Dai, D. F. Han, L. P. Han, Y. Y. Fan, J. N. Xu, D. X. Han and L. Niu, *Anal. Chem.*, 2019, **91**, 10657–10662.
6 M. Zhao, G. C. Fan, J. J. Chen, J. J. Shi and J. J. Zhu, *Anal. Chem.*, 2015, **87**, 12340–12347.
7 G. C. Fan, L. Han, H. Zhu, J. R. Zhang and J. J. Zhu, *Anal. Chem.*, 2014, **86**, 12398–12405.
8 P. P. Li, Y. Cao, C. J. Mao, B. K. Jin and J. J. Zhu, *Anal. Chem.*, 2019, **91**, 1563–1570.
9 Y. H. Zhang, Y. N. Zheng, M. J. Li, T. Hu, R. Yuan and S. P. Wei, *Anal. Chem.*, 2018, **90**, 12278–12283.
10 R. Wu, G. C. Fan, L. P. Jiang and J. J. Zhu, *ACS Appl. Mater. Interfaces*, 2018, **10**, 4429–4438.

11 Z. B. Xiao, Z. L. Li, P. Y. Li, X. P. Meng and R. H. Wang, *ACS Nano*, 2019, **13**, 3608–3617.
12 J. R. Ran, G. P. Gao, F. T. Li, T. Y. Ma, A. J. Du and S. Z. Qiao, *Nat. Commun.*, 2017, **8**, 13907.
13 R. J. Meng, J. M. Huang, Y. T. Feng, L. H. Zu, C. X. Peng, L. R. Zheng, L. Zheng, Z. B. Chen, G. L. Liu, B. J. Chen, Y. L. Mi and J. H. Yang, *Adv. Energy Mater.*, 2018, **8**, 1801514.
14 Y. J. Xu, S. Wang, J. Yang, B. Han, R. Nie, J. X. Wang, J. G. Wang and H. W. Jing, *Nano Energy*, 2018, **51**, 442–450.
15 H. Wang, Y. Wu, T. Xiao, X. Z. Yuan, G. M. Zeng, W. G. Tu, S. Y. Wu, H. Y. Lee, Y. Z. Tan and J. W. Chew, *Appl. Catal., B*, 2018, **233**, 213–225.
16 S. C. Wang, P. Chen, J. H. Yun, Y. X. Hu and L. Z. Wang, *Angew. Chem., Int. Ed.*, 2017, **56**, 8500–8504.
17 S. C. Wang, P. Chen, Y. Bai, J. H. Yun, G. Liu and L. Z. Wang, *Adv. Mater.*, 2018, **30**, 1800486.
18 S. W. Cao, B. J. Shen, T. Tong, J. W. Fu and J. G. Yu, *Adv. Funct. Mater.*, 2018, **28**, 1800136.
19 H. Wang, Y. M. Sun, Y. Wu, W. G. Tu, S. Y. Wu, X. Z. Yuan, G. M. Zeng, Z. C. Xu, S. Z. Li and J. W. Chew, *Appl. Catal., B*, 2019, **245**, 290–301.
20 B. Anasori, M. R. Lukatskaya and Y. Gogotsi, *Nat. Rev. Mater.*, 2017, **2**, 16098.
21 T. Cai, L. L. Wang, Y. T. Liu, S. Q. Zhang, W. Y. Dong, H. Chen, X. Y. Yi, J. L. Yuan, X. N. Xia, C. B. Liu and S. L. Luo, *Appl. Catal., B*, 2018, **239**, 545–554.
22 Z. C. Zhuang, Y. Li, Z. L. Li, F. Lv, Z. Q. Lang, K. N. Zhao, L. Zhou, L. Moskaleva, S. J. Guo and L. Q. Mai, *Angew. Chem., Int. Ed.*, 2018, **57**, 496–500.
23 H. M. Da, Y. L. Liu, M. J. Li, R. Yuan, H. Y. Liu and Y. Q. Chai, *Chem. Commun.*, 2019, **55**, 8076–8078.
24 S. Dehghani, R. Nosrati, M. Yousefi, A. Nezami, F. Soltani, S. M. Taghdisi, K. Abnous, M. Alibolandi and M. Ramezani, *Biosens. Bioelectron.*, 2018, **110**, 23–37.
25 H. M. Da, H. Y. Liu, Y. N. Zheng, R. Yuan and Y. Q. Chai, *Biosens. Bioelectron.*, 2018, **101**, 213–218.

